Particle-induced morphological modification of Al alloy equiaxed dendrites revealed by sub-second *in situ* microtomography

Authors: R. Daudin*[, 1], S.Terzi[2,3], P.Lhuissier[1], J. Tamayo[4], M. Scheel[3,5], N. Hari Babu[4], D.G. Eskin[4] and L. Salvo[1]

[1]Univ. Grenoble Alpes, CNRS, SIMAP, F-38000 Grenoble, France

[2]European Space Agency, ESTEC, TEC-TS, EPN Campus, CS20156, 38042 Grenoble Cedex 9, France

[3]ESRF-The European Synchrotron, CS40220, 38043 Grenoble Cedex 9, France

[4]Brunel Centre for Solidification Technology, Brunel University London, Uxbridge UB8 3PH

[5]Société civile Synchrotron SOLEIL, Saint-Aubin - BP 48, 91192 Gif-sur-Yvette CEDEX, France

*Corresponding author: remi.daudin@simap.grenoble-inp.fr

Abstract

The study of dendritic growth is a challenging topic at the heart of intense research in material science. Understanding such processes is of prime importance as it helps predicting the final microstructure governing material properties. In the specific case of the design of metal-matrix nanocomposites (MMNCs), the addition of nano-sized particles inside the metallic melt increases the complexity as their influence on the growth morphology of dendrites is not yet fully understood. In the present experimental study, we use *in situ* X-ray tomography imaging with very high temporal resolution (0.35 s per 3D image) coupled with *in situ* ultrasonic melt homogenisation to record, in 3D and real time, the free growth at high cooling rates (~2 $K.s^{-1}$) of equiaxed dendrites in an AA6082 alloy containing Y_2O_3 nanoparticles. The careful 3D analysis of the dendrite morphologies as well as their solidification dynamics reveals that in the case of well-dispersed particles, dendrite equiaxed growth occurs through complex hyper-branched morphologies. Such behaviour is believed to arise from particle-induced modification of the solidification processes at the origin of multiple splitting, branching and curving mechanisms of the dendrite arms. These results shed light on long-standing empirical and modelling statements and open new ways for direct investigation of equiaxed growth in metallic alloys and composites.

Keywords: Al alloys; Metal matrix composites (MMCs); Synchrotron radiation computed tomography; *Solidification microstructures; Equiaxed dendrites morphologies.*

1. Introduction

Describing and understanding accurately the complexity and the diversity of dendrites morphologies is a challenging fundamental physical problem related to liquid-solid phase transition [1] and is of high practical interest as it helps predicting the final microstructure that governs the materials properties. Many models have been derived and completed over the years to describe the steady-state dendrite growth, from the early analytical model of Ivantsov [2] to the recent multiscale dendritic needle network model [3,4] and the widely used phase field approach [5–9]. Until recently, only transparent organics that are thought to "freeze like metals" [10] could be used as experimental validation but could only provide 2D observations [11–13] and recent outcomes pointed out that metallic alloys may present more complex behaviour [8,14]. Because of technical issues concerning the time needed to collect images *in situ*, free growth stages are mainly accessible by radiography (2D) [15–17,4] and X-ray tomography (3D) is often limited to slow cooling rates [14,18–20]. Very few studies report *in situ* tomography acquisition during dendrites free growth at relatively high cooling rates [21–23]. While our understanding on dendrites growth is constantly improving, most advanced models or simulation techniques still cannot fully describe experimental results [24] and lack 3D *in situ* experimental dataset in metals to be improved.

For more complex materials, such as metal-matrix nanocomposites (MMNCs) that are promising materials in applications where lightweighting and high strength are important issues [25], interaction between the solidification front and the particles requires consideration. If a consensus seems to exist for a planar front interfering with a spherical particle [26–28] , only few studies focus on dendrite tips and particles interactions [6,11,29]. Using 2D phase field simulations, Granazy *et al* showed that particles can significantly modify the equiaxed dendrites morphology [6,7]. Experimental evidence of such mechanisms in metals, in 3D, is missing mainly due to the fact that natural aggregation of the particles in the melt hinders clear comparison [18]. The size of aggregates can be significantly reduced by applying

intense ultrasonic melt treatment (UST) leading to an excellent dispersion of particles within the melt prior to solidification [26,30,31]. By adapting this technique on a synchrotron tomography beamline, we managed to observe experimentally in 3D the free growth of equiaxed dendrites in a liquid AA6082 alloy containing Y_2O_3 nanoparticles. We show that the size and the distribution variations of the nanoparticles lead either to dense globular or complex hyper-branched dendrites. These experimental results are confronted to reported numerical works [6–8,29,32] and provide valuable insights for crystal growth and development of low-alloy Al MMNCs

2. Experimental methods

2.1. Sample preparation

The material was processed by BCAST at Brunel University London. The incorporation of 1wt% Y_2O_3 particles (~ 500 nm) in the molten AA6082 (composition in wt%: 0.7–1.3% Si, 0.4–1% Mn, 0.6–1.2% Mg, 0.5% Fe, 0.25% Cr,0.2% Zn, 0.1% Cu, 0.1% Ti.) matrix was performed under mechanical stirring (Ti impeller at 400 rpm). Ultrasonic melt treatment was applied for 5 minutes at a frequency of 17.5 kHz with a Nb sonotrode (amplitude nul-to-peak of 20 μm). The detailed procedure can be found elsewhere [33]. The samples were machined into cylindrical-shaped specimens of 5 mm in diameter fitting to the crucible inside which they were further melted.

2.2. Experimental apparatus

The sonication device is composed of a transducer, a booster and a sonotrode. Both transducer and booster are commercially available parts (MPI-ultrasonics) whereas the probe part was especially designed to efficiently apply ultrasound to molten millimetre-size Aluminium composite samples during *in situ* tomography imaging (Figure 1). The system is based on a principle where the fine sonotrode is introduced inside a small crucible. Whereas conventional designs for large sonotrodes usually include

probes composed of one or two sections, the present sonotrode is composed of three different sections. Indeed, the reduction of the tip diameter increases the constraints at the reduction section leading to failure after short time of use. Using COMSOL sowftware, a three-section sonotrode was modelled for a targeted eigenfrequency of 20 kHz using a two dimensional axisymmetric approach. The total length (145 mm) and the different lengths corresponding to the different sections with fixed diameters (12, 6 and 3 mm) were computed by minimizing and balancing the stresses along the ultrasonic horn. The Ti sonotrode was then machined at the lab according to the computational results obtained. The crucibles containing the 5 mm samples are made of alumina and were glued at the top of an alumina rod fixed on a rotating stage. An induction furnace consisted of a copper coil placed around the crucible allowing the samples to be remelted. The temperature was measured using a pyrometer monitoring the area imaged during solidification. The sonotrode was screwed on the sonication device that was mounted on a translation stage above the crucible. The vertical displacement of the ultrasonic horn was remotely controlled allowing its immersion inside the melt for ultrasonic treatments and its withdrawing quickly after US processing. The frequency, amplitude and duration of ultrasounds were controlled using an MPI Labview program.

2.3. Experimental procedure

The experimental procedure consisted in three stages. First, a AA6082 Al alloy either containing or not Y_2O_3 nanoparticles was melted with an induction furnace. Second, in the fully liquid state, ultrasonic treatment (30 s at a frequency of 19.6 kHz) was either applied or not through the dedicated Ti sonotrode. Finally, the sonotrode was withdrawn, the induction furnace switched off letting the sample cool naturally and ultrafast *in situ* microtomography was performed. The unique combination of high energy and high flux provided by the ESRF-ID15 beamline enables the examination of the complete solidification sequence inside 5 mm thick samples at cooling rates in between 1.5 and 3 $K.s^{-1}$. The time range during which useful information on free growth mechanisms was accessible was very short (~1.5

s) but sufficient to unravel the impact of UST on the size and distribution of Y_2O_3 nanoparticles and consequently on the dendrite growth morphologies. Additional results regarding samples without nanoparticles are discussed in Supplementary Material.

2.4. In situ tomography data acquisition

In situ tomography was performed at the ID15 beamline at ESRF during solidification after ultrasonic melt treatment. A dedicated optic system composed of an x10 objective and a LuAG scintillator converting the X-ray light into visible light were placed at front of the camera. The latter was a PCO-Dimax camera allowing ultrafast acquisition of images. The tomography scans were recorded during the solidification of the sample from the liquid state. The induction furnace was powered down right after and continuous acquisition was performed during solidification with a cooling rate of the order of 2 $K.s^{-1}$ by recording 52000 projections with an exposure time of 0.35 ms, a pixel size of 1.1 µm and a field of view of 1200x400 voxels (1.32 x 0.44 mm^3). The angular projection step was set to record 1000 images over 180° leading to a scan time of 0.35s. Continuous acquisition was performed meaning that there was no delay between two scans. 52 scans were recorded in the camera memory leading to 32 Gb of data. Data was then downloaded from camera memory to disks while another sample was mounted.

2.5. Image reconstruction and processing

The reconstructed 3D volumes were then obtained by applying filtered back-projection algorithms with Paganin algorithms [34] (δ/β of 150). The 3D reconstructed images were corrected with 3D median filters, bilateral filters and non local mean filters as well as manually cleaned from noise pollution allowing efficient segmentation for quantitative analysis (Supplementary Figure 5) with regular imaging tools such as ImageJ and Avizo.

3. Results

3.1. Nucleation and growth

The dendrite morphologies observed during the solidification of the AA6082+Y_2O_3 nanocomposites with and without UST are displayed in Figure 2 where 2D cross-sections extracted from the 3D images are shown. At 1 s, in both cases, the solid nucleants are very small, move in the liquid and consequently cannot be reconstructed clearly. At 4.35 s, there are few, small and separated dendrites in the field of view whose mutual interaction is considered as negligible: this is the free growth stage at the heart of the present study. With the presence of Y_2O_3 nanoparticles acting as nucleates inside the bulk of the material, equiaxed growth is the main solidification mode. Without UST, the particles are structured into large clusters of particles associated with porosity (Supplementary Figure 4) that can easily trigger nucleation and the developing dendrites exhibit large round-shaped arms. Performing UST breaks these particle aggregates and suppresses porosity (section 3.2, Figure 3). The nucleation frequency is estimated to be reduced by a factor 2 which is likely to be related with the suppression of these large and potent clusters (Figure 2). With UST, solidification also occurs through equiaxed dendrites but their arms appear thinner, more branched and sometimes curved. The dendrites selected for more in depth quantitative 3D morphology analysis (sections 3.3 and 3.4) are highlighted by boxes.

At 5.75 s, the solid fraction is too high to reasonably assume free growth but the 2D slices clearly underline the difference of the developing microstructures. Moreover aggregates of particles are visible in the sample solidified without UST. Although quantitative analysis within a reasonable error range could not be conducted, the intermetallic phase containing heavy elements and solidifying at the latest stage between the dendrites arms, seems thinner and more homogeneously distributed (when UST is performed) and is thus a footprint of the solidification of the hyper-branched dendrites.

3.2. Porosity content

At 4.35 s in Figure 2, porosity is already visible in the solidifying sample when UST was not performed but represents only 0.02% in volume fraction (red curve, Figure 3a). During further cooling, the sudden

increase in porosity content on the red curve arises when dissolved hydrogen present in the aluminium melt diffuses inside the pores due to a decrease of hydrogen solubility in the melt during solidification [35]. The size of pores then raises leading to an increase in the overall volume fraction of defects in the solid state (1% in volume fraction). When UST is performed, the melt is homogenized and ultrasonic degassing processes occur [30] leading to the suppression of residual porosity and hence defects in the solid state (Figure 3b). Due to the presence of very few pores when UST is performed, only the final state content was quantitatively analyzed and was found to remain as low as 0.015% in volume fraction.

3.3. Dendrites 3D morphologies

Careful and sustained efforts using reconstruction algorithms and post-processing filters (Supplementary Figure 5) were applied to extract the accurate 3D morphologies of representative dendrites (in boxes in Figure 2). The ratio between the dendrite volume (V_d) and the Convex-Hull envelope containing it (V_e) determines the dendrites compactness and is compared for equivalent solidification states (Figure 4a and Figure 4b). Values of 40% and 15% are found for the nanocomposite processed without UST and with UST, respectively. The latter thus solidifies through less compact dendrites. Moreover, the mean thickness of the dendrites arms, obtained by 3D granulometry analysis (Supplementary Figure 6) is much smaller in the sample with UST (11±5 µm) than in the sample without UST (30±7.5 µm). The 3D rendering of the local surface curvedness (Figure 4c and Figure 4d) clearly illustrates that without UST, the dendrites arms present less pronounced curved surfaces, even at their tips whereas with UST, the curvedness of the dendrites arms is greatly enhanced. This is confirmed by the Interface Shape Distribution [14,36] (ISD) of local shape factor S and local curvedness C pairs in Figure 4e and Figure 4f. The local curvedness C is given by $C=1/2\sqrt{(\kappa_1^2+\kappa_2^2)}$ with κ_1 and κ_2 the principal curvatures of the considered surface patch obtained by discretizing the dendrites surfaces. The convention used here is $\kappa_2>\kappa_1$ and the value of C indicates the curvature magnitude of the patch, with C=0 for a perfectly flat surface. The shape factor S given by $S= 2/\pi*\text{atan}(\kappa_1+\kappa_2/\kappa_2-\kappa_1)$ indicating the local shape of the interface

with S=±1 for spheres, S=±0.5 for cylinders and S=0 for hyperbola with positive (respectively negative) values indicating that concavity is pointing towards the solid phase (respectively liquid phase).

The two ISDs present similar global shapes with almost all the intensity distributed in the positive side of S because the concavity of dendrites points towards the solid. For both ISDs, the highest density of probability is found for S ∈ [0.4-0.6] corresponding to the cylindrical shape of dendrite arms. However, without UST, C values are centred around 0.10 μm^{-1} whereas a value of 0.22 μm^{-1} is found when UST is performed, confirming that dendrites arms are thinner. More generally the whole ISD intensity is shifted towards low C values in absence of UST, attesting for the overall lower curvature of the different arms. More importantly, a non-negligible part of the intensity spans towards S values ranging from 0 to 0.4 indicating that dendrite arms are more globular when UST are not applied.

3.4. Solidification dynamics in 3D

In situ tomography offers a unique possibility to capture the solidification dynamics in 3D. Indeed, the comparison of the 3D solid-liquid interface distribution of the selected dendrites between two time steps makes possible the determination of the 3D solidification front velocity field (Figure 5a and **Figure 5**b) representing the local velocity (V_{local}). Evaluating the mean 3D growth rate consists in applying a V_{local} threshold value (estimated to 30 $\mu m.s^{-1}$) below which the velocity corresponds to solid growth far from the tips. Calculation of weighted means and weighted deviations of V_{local} (histograms in Figure 5) yields 41±12 $\mu m.s^{-1}$ (no UST) and 51±20 $\mu m.s^{-1}$ (UST) highlighting a fairly similar mean growth velocity between the two cases but with much higher dispersion when ultrasound is applied with some arm tips growing faster than 100 $\mu m.s^{-1}$ (V_{tip}). For a given macroscopic undercooling, it is expected that all arms would grow with the same R_{tip} and V_{tip} values [1,3,15] but interestingly for the treated sample (UST), different arm tips belonging to the same dendrite are observed to grow at significantly different velocities. In insets of Figure 5, the log-log plots of (R_{tip}, V_{tip}) pairs measured on selected dendrites show a transition from $V_{tip}*R_{tip} = cst$ (no UST) to $V_{tip}^{1.7}*R_{tip} = cst$ (with UST). The difference in the power-law exponents relating V_{tip} and R_{tip} calculated for the two representative dendrites, while not being a tell-

tale result on its own, indirectly reveals the impact of differences in size and distribution of the Y_2O_3. Different key parameters controlling dendrites morphology can potentially be locally modified by the presence of these particles, in several ways, as discussed hereafter.

4. Discussion

The dendrite tip velocity V_{tip} is not constant over time in the solidification of the ultrasonically processed AA6082+Y_2O_3 sample (Figure 6a). Such variation was reported in simulations of thermal dendrites in the presence of particles. The heat flow is locally modified in the surrounding of the particles inducing dendrite tip acceleration or deceleration depending on the thermal property of the particles. Dendrite curving and splitting are potential outcomes of this mechanism [29].

In alloys however, the solid growth is mainly governed by solutal effects. The influence of the particle is therefore believed to rather be on the solute diffusion ahead of the growth front [11]. Particles can indeed restrain the diffusion of solute creating local compositional heterogeneities and variations of driving force. The change with time of the growth velocity as well as arm bending can then be naturally explained by the fact that dendrites are growing into a field of particle-induced inhomogeneities [6,7]. Tip-splitting can also be generated through this mechanism when a groove enriched in solute is created at the growth front by a non-engulfed particle/aggregate that induces solute pile-up [11,26] (Supplementary Figure 11).

The presence of particles may also have an influence on side-branching. Glicksman *et al* recently developed a determinist approach of this mechanism where the capillary forces at the surface of an arm can induce local surface rotation, at specific locations (instead of random) and initiate branching [32,37]. With a more deformed shape of dendrite arms, the number and position of these nucleation points may be greatly impacted which can play a role in increasing the complexity of morphologies. The role of capillary forces is however constrained to the formation of arms, their growth being then controlled by solute transport.

Branching and change in growth direction were also found to be a consequence of a compositional dependence of interfacial anisotropy. Using phase field simulation, Haxhimali *et al* revealed the continuous variation of the growth direction not limited to a finite number of crystallographic orientations [8]. Related mechanisms were observed experimentally in columnar growth of Al-Zn [8], Al-Cu [24] and noteworthy in the present AA6082 without particles and UST (Supplementary Figure 2) where secondary arms growing in regions increasing in solute content exhibit a tendency to curve. The directionality of columnar growth induces however a certain symmetry and regularity in growth pattern. Here, the equiaxed growth triggered by the Y_2O_3 particles is therefore even less constrained and a greater degree of freedom is left to the dendrite arms for following different directions dictated by the local variation of solute content. Modifying the number and spatial distribution of heterogeneities in the melt can certainly have an influence on the morphology of the dendrites growing in such media. Branching and splitting events are then more frequent when the field of particles is better dispersed by performing UST leading to the hyper-branched structure shown in Figure 4b and Figure **6**b.

Direct interactions of particles with dendrite tips was also studied in the metallic Ni-Cu system by phase field simulation by Gránásy *et al.* who revealed that immobile particles can deviate the tip by promoting growth front nucleation (GFN), minimizing the interface energy and leading to "dizzy" polycrystalline microstructures [6]. The arm of the present study highlighted in Figure 6c undergoes a comparable deflection from its initial growing axis inducing a curved dendrite. Considering that the deflection is large (~30°) and that the grain size is comparable to the size of the dendrites (150~200 µm, Supplementary Figure 12), such direct mechanisms, if plausible, are supposed to be limited. Again, the hyper-branched morphology is thus rather related to local modifications of the solute diffusion behaviour, likely influenced by the distribution of the particles, promoting single-crystal dendrite as also obtained numerically by Gránásy *et al* [7]. At the time, experimental comparison was taken with solidification of 2D transparent organics that only showed elementary mechanisms [6,11,13] and were stated to be general processes (Figure 7). At present, resolution-limited tomography experiments cannot provide clear location of such small and moving particles, even at high acquisition rates, but can rather bring insights in the behaviour of low-alloyed Al materials and during free equiaxed growth. The

comparison between Figure 7c-d andFigure 7e-f highlights the morphological similarities between the present experimental results and the simulation results obtained by Gránásy *et al* [7]. While fundamental mechanisms are believed to differ from transparent organics and simulations, the present results support manifold mechanisms but this time obtained experimentally (for the first time in 3D), with small and highly dispersed nanoparticles in a conventional metallic melt.

5. Conclusion

To conclude, the development of branched palm-tree structures (Figure 7) through multiple splitting and branching events indicates how particles, that are free to move compared to fixed particles in simulations results [6,7,29] or confined particles in 2D experiments [6,11], influence the dendrites growth. Indeed, in addition to directly influencing nucleation, they are more likely to have an indirect impact (local variation of solute content) rather than a direct impact (promotion of GFN) on crystal growth.

With constant improvements of experimental apparatus and light sources, such work demonstrates the promising potential and essential knowledge that can be gained by *in situ* characterisation. It clearly demonstrates that free crystal growth in low-alloyed Al melt containing particles, is far from ideal models and requires in depth experimental investigation, especially in equiaxed growth. It also corroborates the necessity to investigate solidification of metallic alloys directly instead of relying on their transparent counterparts [14] and provides valuable information for theoretical or computational investigations as well as for practical considerations concerning processing of MMNCs.

Acknowledgment

The authors wish to acknowledge financial support from the ExoMet Project, which is co-funded by the European Commission in the 7th Framework Program (contract FP7-NMP3-LA-2012-280421) by the European Space Agency and by the individual partner organizations.

They also wish to acknowledge the ESRF-MA1876 long term project, E. Boller and A. Rack from ESRF-ID19 beamline, for providing strong support concerning the development and test of the dedicated set-up as well as facilitating reconstruction procedure and 3D analysis.

Technical and scientific supports provided by W. Sillekens and D. Jarvis from the European Space Agency was also greatly appreciated.

References

[1] M. Rappaz, J.A. Dantzig, Solidification, EPFL-Press, 2009.

[2] G.P. Ivantsov, Temperature field around a spheroidal, cylindrical and acicular crystal growing in a supercooled melt., Dokl. Akad. Nauk SSSR. 58 (1947) 567–569.

[3] D. Tourret, A. Karma, Multiscale dendritic needle network model of alloy solidification, Acta Mater. 61 (2013) 6474–6491. doi:10.1016/j.actamat.2013.07.026.

[4] L. Sturz, A. Theofilatos, Two-dimensional multi-scale dendrite needle network modeling and x-ray radiography of equiaxed alloy solidification in grain-refined Al-3.5 wt-%Ni, Acta Mater. 117 (2016) 356–370. doi:10.1016/j.actamat.2016.06.005.

[5] R. Kobayashi, Modeling and numerical simulations of dendritic crystal growth, Phys. Nonlinear Phenom. 63 (1993) 410–423. doi:10.1016/0167-2789(93)90120-P.

[6] L. Gránásy, T. Pusztai, J.A. Warren, J.F. Douglas, T. Börzsönyi, V. Ferreiro, Growth of "dizzy dendrites" in a random field of foreign particles, Nat. Mater. 2 (2003) 92–96. doi:10.1038/nmat815.

[7] L. Gránásy, T. Pusztai, T. Börzsönyi, J.A. Warren, J.F. Douglas, A general mechanism of polycrystalline growth, Nat. Mater. 3 (2004) 645–650. doi:10.1038/nmat1190.

[8] T. Haxhimali, A. Karma, F. Gonzales, M. Rappaz, Orientation selection in dendritic evolution, Nat. Mater. 5 (2006) 660. doi:10.1038/nmat1693.

[9] Y. Chen, D.Z. Li, B. Billia, H. Nguyen-Thi, X.B. Qi, N.M. Xiao, Quantitative Phase-field Simulation of Dendritic Equiaxed Growth and Comparison with in Situ Observation on Al – 4 wt.% Cu Alloy by Means of Synchrotron X-ray Radiography, ISIJ Int. 54 (2014) 445–451. doi:10.2355/isijinternational.54.445.

[10] K.A. Jackson, J.D. Hunt, Transparent compounds that freeze like metals, Acta Metall. 13 (1965) 1212–1215. doi:10.1016/0001-6160(65)90061-1.

[11] J.A. Sekhar, R. Trivedi, Solidification microstructure evolution in the presence of inert particles, Mater. Sci. Eng. A. 147 (1991) 9–21. doi:10.1016/0921-5093(91)90800-3.

[12] B. Utter, E. Bodenschatz, Dynamics of low anisotropy morphologies in directional solidification, Phys. Rev. E. 66 (2002) 51604. doi:10.1103/PhysRevE.66.051604.

[13] V. Fleury, Branched fractal patterns in non-equilibrium electrochemical deposition from oscillatory nucleation and growth, Nature. 390 (1997) 145–148. doi:10.1038/36522.

[14] J.W. Gibbs, K.A. Mohan, E.B. Gulsoy, A.J. Shahani, X. Xiao, C.A. Bouman, M. De Graef, P.W. Voorhees, The Three-Dimensional Morphology of Growing Dendrites, Sci. Rep. 5 (2015) 11824. doi:10.1038/srep11824.

[15] A. Bogno, H. Nguyen-Thi, G. Reinhart, B. Billia, J. Baruchel, Growth and interaction of dendritic equiaxed grains: In situ characterization by synchrotron X-ray radiography, Acta Mater. 61 (2013) 1303–1315. doi:10.1016/j.actamat.2012.11.008.

[16] Y. Chen, B. Billia, D.Z. Li, H. Nguyen-Thi, N.M. Xiao, A.-A. Bogno, Tip-splitting instability and transition to seaweed growth during alloy solidification in anisotropically preferred growth direction, Acta Mater. 66 (2014) 219–231. doi:10.1016/j.actamat.2013.11.069.

[17] A. Prasad, E. Liotti, S.D. McDonald, K. Nogita, H. Yasuda, P.S. Grant, D.H. StJohn, Real-time synchrotron x-ray observations of equiaxed solidification of aluminium alloys and implications for modelling, IOP Conf. Ser. Mater. Sci. Eng. 84 (2015) 12014. doi:10.1088/1757-899X/84/1/012014.

[18] R. Daudin, S. Terzi, P. Lhuissier, L. Salvo, E. Boller, Remelting and solidification of a 6082 Al alloy containing submicron yttria particles: 4D experimental study by in situ X-ray microtomography, Mater. Des. 87 (2015) 313–317. doi:10.1016/j.matdes.2015.07.141.

[19] N. Limodin, L. Salvo, E. Boller, M. Suéry, M. Felberbaum, S. Gailliègue, K. Madi, In situ and real-time 3-D microtomography investigation of dendritic solidification in an Al–10 wt.% Cu alloy, Acta Mater. 57 (2009) 2300–2310. doi:10.1016/j.actamat.2009.01.035.

[20] S. Shuai, E. Guo, A.B. Phillion, M.D. Callaghan, T. Jing, P.D. Lee, Fast synchrotron X-ray tomographic quantification of dendrite evolution during the solidification of MgSn alloys, Acta Mater. 118 (2016) 260–269. doi:10.1016/j.actamat.2016.07.047.

[21] L. Salvo, M. DiMichiel, M. Scheel, P. Lhuissier, B. Mireux, M. Suéry, Ultra fast in situ X-ray micro-tomography : application to solidification of aluminium alloys, Mater. Sci. Forum. 706–709 (2012) 1713–1718. doi:10.4028/www.scientific.net/MSF.706-709.1713.

[22] B. Cai, J. Wang, A. Kao, K. Pericleous, A.B. Phillion, R.C. Atwood, P.D. Lee, 4D synchrotron X-ray tomographic quantification of the transition from cellular to dendrite growth during directional solidification, Acta Mater. 117 (2016) 160–169. doi:10.1016/j.actamat.2016.07.002.

[23] A.G. Murphy, W.U. Mirihanage, D.J. Browne, R.H. Mathiesen, Equiaxed dendritic solidification and grain refiner potency characterised through in situ X-radiography, Acta Mater. 95 (2015) 83–89. doi:10.1016/j.actamat.2015.04.060.

[24] J. Friedli, J.L. Fife, P. Di Napoli, M. Rappaz, Dendritic Growth Morphologies in Al-Zn Alloys—Part I: X-ray Tomographic Microscopy, Metall. Mater. Trans. A. 44 (2013) 5522–5531. doi:10.1007/s11661-013-1912-7.

[25] W.H. Sillekens, D.J. Jarvis, A. Vorozhtsov, V. Bojarevics, C.F. Badini, M. Pavese, S. Terzi, L. Salvo, L. Katsarou, H. Dieringa, The ExoMet Project: EU/ESA Research on High-Performance

Light-Metal Alloys and Nanocomposites, Metall. Mater. Trans. A. 45 (2014) 3349–3361. doi:10.1007/s11661-014-2321-2.

[26] X.-H. Chen, H. Yan, Solid–liquid interface dynamics during solidification of Al 7075–Al2O3np based metal matrix composites, Mater. Des. 94 (2016) 148–158. doi:10.1016/j.matdes.2016.01.042.

[27] D.M. Stefanescu, A. Moitra, A.S. Kacar, B.K. Dhindaw, The influence of buoyant forces and volume fraction of particles on the particle pushing/entrapment transition during directional solidification of Al/SiC and Al/graphite composites, Metall. Trans. A. 21 (1990) 231–239. doi:10.1007/BF02656440.

[28] J.B. Ferguson, G. Kaptay, B.F. Schultz, P.K. Rohatgi, K. Cho, C.-S. Kim, Brownian Motion Effects on Particle Pushing and Engulfment During Solidification in Metal-Matrix Composites, Metall. Mater. Trans. A. 45 (2014) 4635–4645. doi:10.1007/s11661-014-2379-x.

[29] Y. Yang, J.W. Garvin, H.S. Udaykumar, Sharp interface simulation of interaction of a growing dendrite with a stationary solid particle, Int. J. Heat Mass Transf. 48 (2005) 5270–5283. doi:10.1016/j.ijheatmasstransfer.2005.07.028.

[30] G.I. Eskin, D.G. Eskin, Ultrasonic Treatment of Light Alloy Melts, Second Edition, CRC Press, 2014.

[31] W. Mirihanage, W. Xu, J. Tamayo-Ariztondo, D. Eskin, M. Garcia-Fernandez, P. Srirangam, P. Lee, Synchrotron radiographic studies of ultrasonic melt processing of metal matrix nano composites, Mater. Lett. 164 (2016) 484–487. doi:10.1016/j.matlet.2015.11.022.

[32] M.E. Glicksman, Mechanism of Dendritic Branching, Metall. Mater. Trans. A. 43 (2011) 391–404. doi:10.1007/s11661-011-0984-5.

[33] D.G. Eskin, S.K.V. Madam, J. Tamayo, S. a. Vorozhtsov, N.H. Babu, A. b. Vorozhtsov, M.& M.S. The Minerals, Application of External Fields to the Development of Aluminum-Based Nanocomposite and Master Alloys, in: TMS2015 Suppl. Proc., Wiley, 2015: pp. 19–24. http://onlinelibrary.wiley.com.gaelnomade.ujf-grenoble.fr/doi/10.1002/9781119093466.ch3/summary (accessed June 30, 2016).

[34] D. Paganin, S.C. Mayo, T.E. Gureyev, P.R. Miller, S.W. Wilkins, Simultaneous phase and amplitude extraction from a single defocused image of a homogeneous object, J. Microsc. 206 (2002) 33–40. doi:10.1046/j.1365-2818.2002.01010.x.

[35] M. Rappaz, Modeling and characterization of grain structures and defects in solidification, Curr. Opin. Solid State Mater. Sci. 20 (2016) 37–45. doi:10.1016/j.cossms.2015.07.002.

[36] D. Kammer, P.W. Voorhees, The morphological evolution of dendritic microstructures during coarsening, Acta Mater. 54 (2006) 1549–1558. doi:10.1016/j.actamat.2005.11.031.

[37] A.M. Mullis, Spontaneous deterministic side-branching behavior in phase-field simulations of equiaxed dendritic growth, J. Appl. Phys. 117 (2015) 114305. doi:10.1063/1.4915278.

Figure captions:

Figure 1 Experimental apparatus. a Schematic drawing of the experimental device. Inset shows the thermal treatment applied to the samples (T_m is the melting temperature). When performed, UST were applied in the fully liquid state. **b** Picture of the experimental equipment.

Figure 2 Solidification of the AA6082+Y_2O_3 alloys processed without (top) and with ultrasonic melt treatment (bottom). For each case, four 2D slices were extracted from the 3D volumes in the fully liquid state (1 s – 920 K), during free growth just after nucleation (4.35 s – 913 K), during "poisoned growth" [17] (5.75 s – 909 K) and in the final solid state (15 s – 790 K). The stripes in the images in the liquid state at 1 s arise because nucleation has just started, the small solid grains are moving and cannot be reconstructed accurately.

Figure 3 Porosity content. a Evolution of the porosity volume fraction during cooling for the AA6082+Y2O3 sample solidified without UST (red) and with UST (green). **b** 3D rendering of the porosity in the solid state.

Figure 4 Full 3D morphologies characterization of representative dendrites: 3D compactness, Surface Curvedness and Interface Shape Distribution. a, b 3D rendering of the dendrites within their Convex Hull Envelope (in grey transparency) without and with UST, respectively. **c**, **d** 3D rendering of the dendrites with colours representing the local curvedness C (μm^{-1}) of the interface without and with UST, respectively. **e, f** Interface Shape Distribution **[14,36]** displaying the probability of finding a patch of surface with a given (S,C) pair value, without and with UST, respectively. The red colours correspond to high probability of (S,C) pairs whereas blue ones correspond to low probability and yellow to intermediate. The colourbar is normalized by the maximum probability. The overall morphological difference is also supported by (κ_1,κ_2) ISD maps (Supplementary Figure 7).

Figure 5 Quantitative 3D analysis of the local velocity field. 3D rendering of the local velocity fields extracted from two successive time steps (4 s and 4.35 s) when UST are not applied (**a**) and applied (**b**). The overall 3D morphologies of the dendrites are conserved in both cases highlighting the accuracy of local velocity computation (Supplementary Figures 8 and 9). The corresponding histograms are given aside, the mean velocity values as well as the deviations values given in text are weighted by the occurrence. The agreement between local curvature C and R_{tip} values is shown in Supplementary Figure 10.

Figure 6 In depth investigation of splitting and curving of dendrites arms (with UST). a Sequence of successive snapshots extracted from the solidification of the 6082+Y_2O_3 after UST. The arrows point toward the region of interest where a splitting event occurs. The velocity of the arm tip (V_{tip}) was extracted by comparing two images between two successive time steps. The corresponding values are reported on the graph as a function of time showing a modification of the tip velocity due to the branching event. The colour rendering is a guide to the eyes for a better contrast between solid and

liquid phase **b** 3D rendering, at different angles, of the well-developed branched palm-tree morphology taken inside the dashed contour in the 2D cross-section. **c** 2D pictures and 3D segmentation showing the growth of a selected arm between 4 s and 4.7 s. The selected arm presents different environment between the two 2D images because the surrounding arms do not all grow in the plan of the images, confirming the necessity of 3D analysis. The segmentation of this arm in 3D reveals that the tip deviation is real and not a 2D cross-sectional misled interpretation.

Figure 7 Temporal progression of experimental and simulated investigations of particles-induced dendrites morphologies. a and **b** illustrate elementary mechanisms revealed by 2D observations of a single particle respectively splitting **[11]** and deviating **[6]** a dendrite in transparent organics. **c** and **d** are 2D phase field simulation results obtained for metals (Ni-Cu system) **[6,7]** supporting the previously experimental evidences but this time reporting manifold mechanisms either by the presence of a large number of particles or by modification of free energy and kinetic coefficient parameter. **e** and **f** are taken from the present experiment highlighting the morphological similarities. The colour rendering is a guide to the eyes for a better contrast between solid and liquid phase. **a** is reprinted from ref **[11]** with permission, Copyright 1991, Elsevier. **b** and **d** are reprinted from ref **[6]** with permission, Copyright 2003, Nature Publishing Group. **c** is reprinted from ref **[7]** with permission, Copyright 2004 , Nature Publishing Group.

Figure(s)

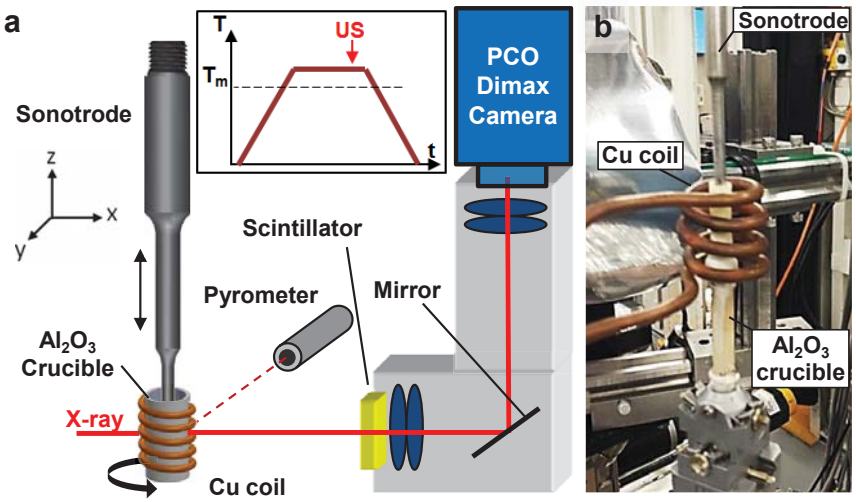

Figure 1 Experimental apparatus and cooling curves. a Schematic drawing of the experimental device. Inset shows the thermal treatment applied to the samples (T_m is the melting temperature). When performed, UST were applied in the fully liquid state. **b** Picture of the experimental equipment.

Figure(s)

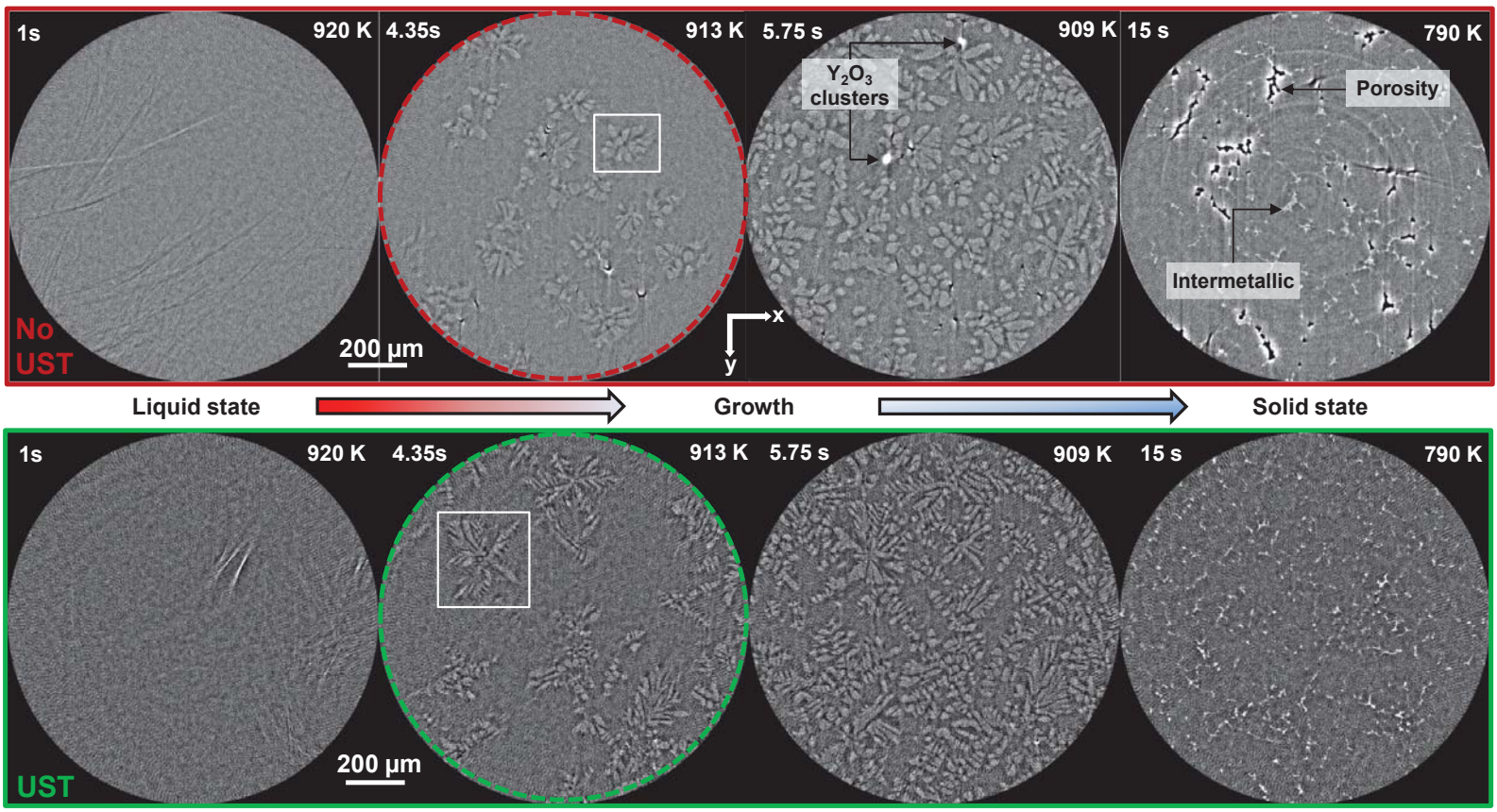

Figure 2 Solidification of the AA6082+Y_2O_3 alloys processed without (top) and with ultrasonic melt treatment (bottom). For each case, four 2D slices were extracted from the 3D volumes in the fully liquid state (1 s – 920 K), during free growth just after nucleation (4.35 s – 913 K), during "poisoned growth" [17] (5.75 s – 909 K) and in the final solid state (15 s – 790 K). The stripes in the images in the liquid state at 1 s arise because nucleation has just started, the small solid grains are moving and cannot be reconstructed accurately.

Figure(s)

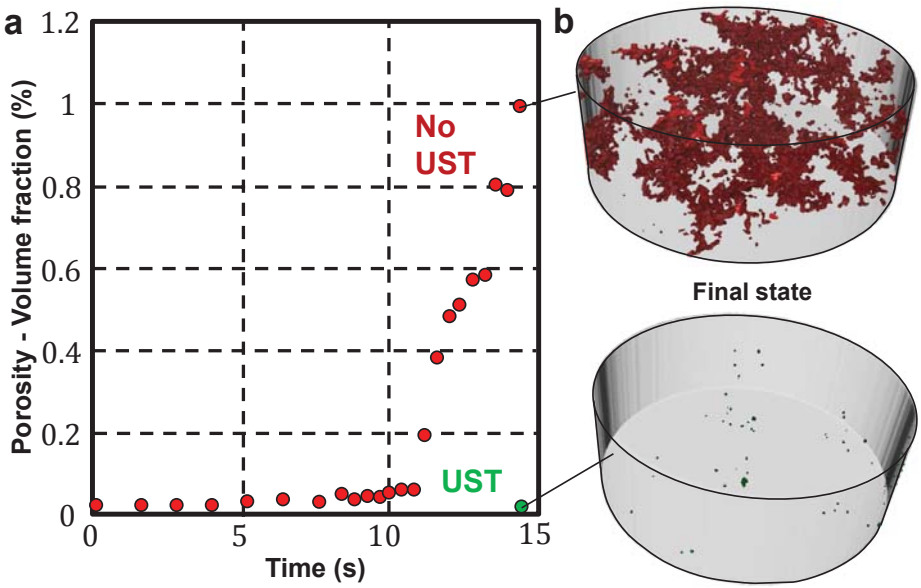

Figure 3 Porosity content. a Evolution of the porosity volume fraction during cooling for the AA6082+Y2O3 sample solidified without UST (red) and with UST (green). **b** 3D rendering of the porosity in the solid state.

Figure(s)

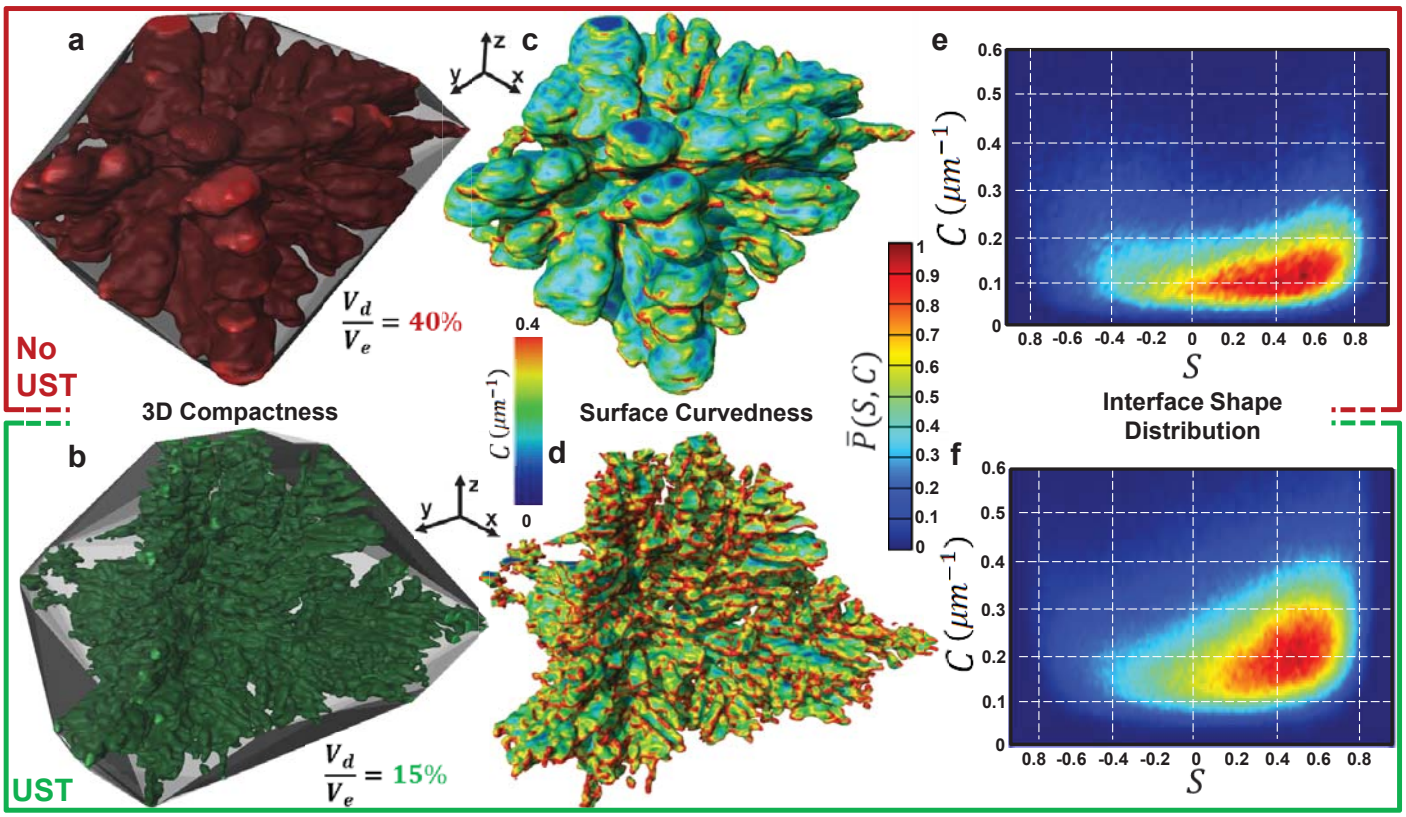

Figure 4 Full 3D morphologies characterization of representative dendrites: 3D compactness, Surface Curvedness and Interface Shape Distribution. a, b 3D rendering of the dendrites within their Convex Hull Envelope (in grey transparency) without and with UST, respectively. **c**, **d** 3D rendering of the dendrites with colours representing the local curvedness C (μm^{-1}) of the interface without and with UST, respectively. **e, f** Interface Shape Distribution **[14,36]** displaying the probability of finding a patch of surface with a given (S,C) pair value, without and with UST, respectively. The red colours correspond to high probability of (S,C) pairs whereas blue ones correspond to low probability and yellow to intermediate. The colourbar is normalized by the maximum probability. The overall morphological difference is also supported by (κ_1,κ_2) ISD maps (Supplementary Figure 7).

Figure(s)

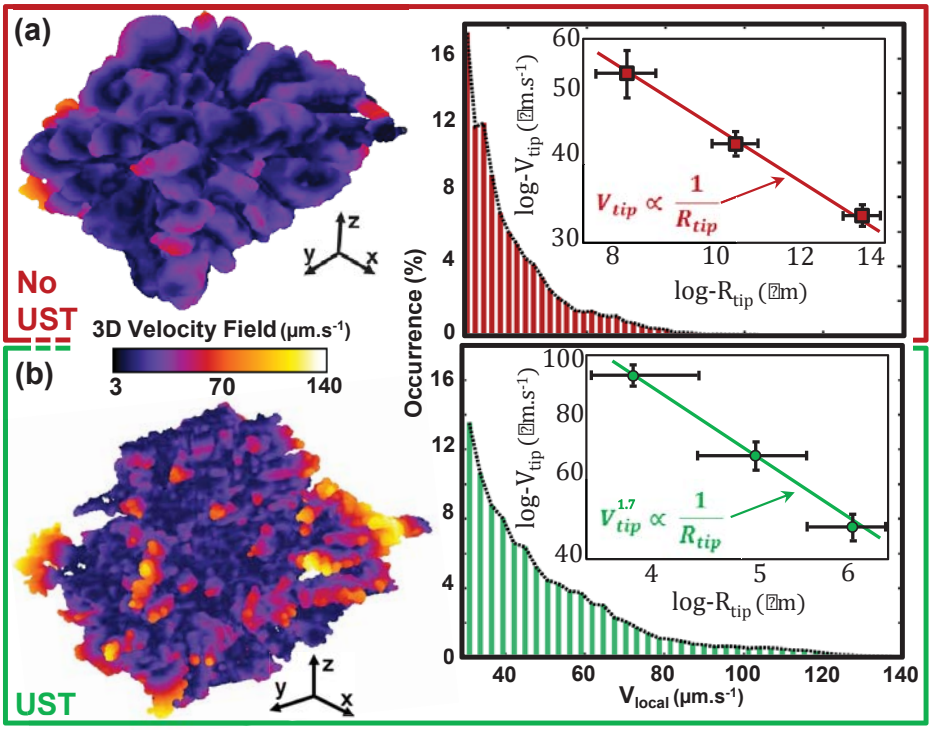

Figure 5 Quantitative 3D analysis of the local velocity field. 3D rendering of the local velocity fields extracted from two successive time steps (4 s and 4.35 s) when UST are not applied (**a**) and applied (**b**). The overall 3D morphologies of the dendrites are conserved in both cases highlighting the accuracy of local velocity computation (Supplementary Figures 8 and 9). The corresponding histograms are given aside, the mean velocity values as well as the deviations values given in text are weighted by the occurrence. The agreement between local curvature C and R_{tip} values is shown in Supplementary Figure 10.

Figure(s)

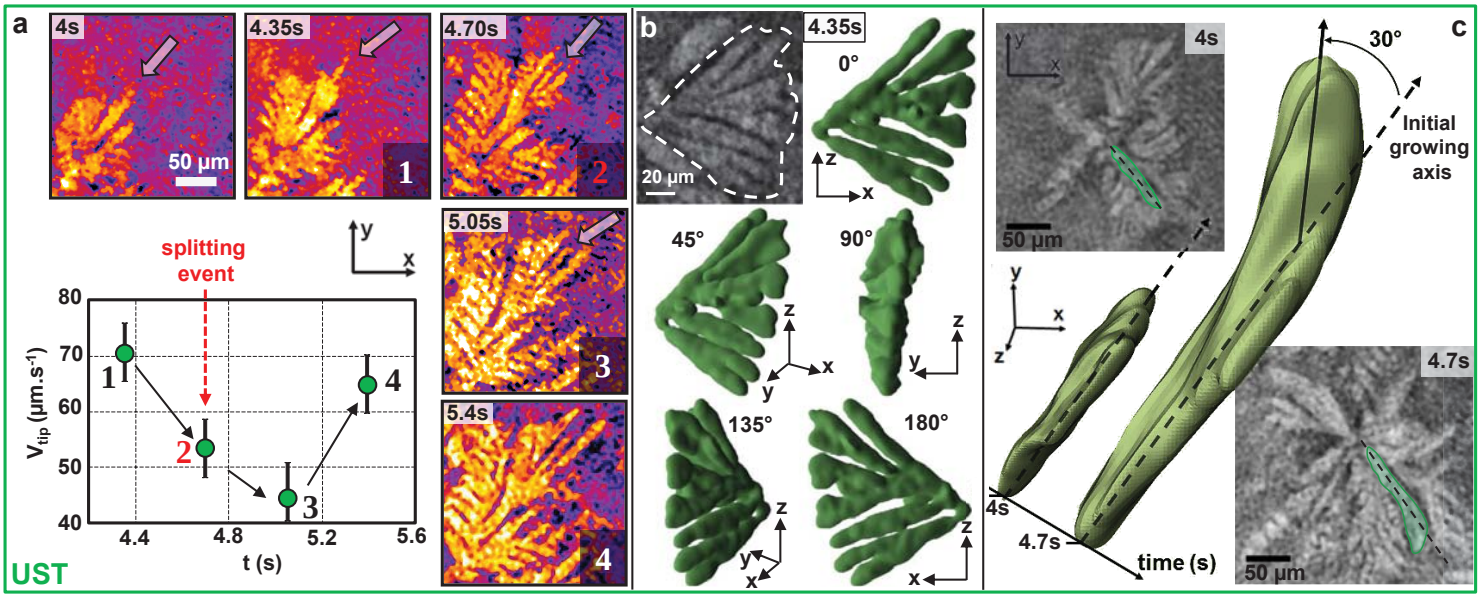

Figure 6 In depth investigation of splitting and curving of dendrites arms (with UST). a Sequence of successive snapshots extracted from the solidification of the 6082+Y_2O_3 after UST. The arrows point toward the region of interest where a splitting event occurs. The velocity of the arm tip (V_{tip}) was extracted by comparing two images between two successive time steps. The corresponding values are reported on the graph as a function of time showing a modification of the tip velocity due to the branching event. The colour rendering is a guide to the eyes for a better contrast between solid and liquid phase **b** 3D rendering, at different angles, of the well-developed branched palm-tree morphology taken inside the dashed contour in the 2D cross-section. **c** 2D pictures and 3D segmentation showing the growth of a selected arm between 4 s and 4.7 s. The selected arm presents different environment between the two 2D images because the surrounding arms do not all grow in the plan of the images, confirming the necessity of 3D analysis. The segmentation of this arm in 3D reveals that the tip deviation is real and not a 2D cross-sectional misled interpretation.

Figure(s)

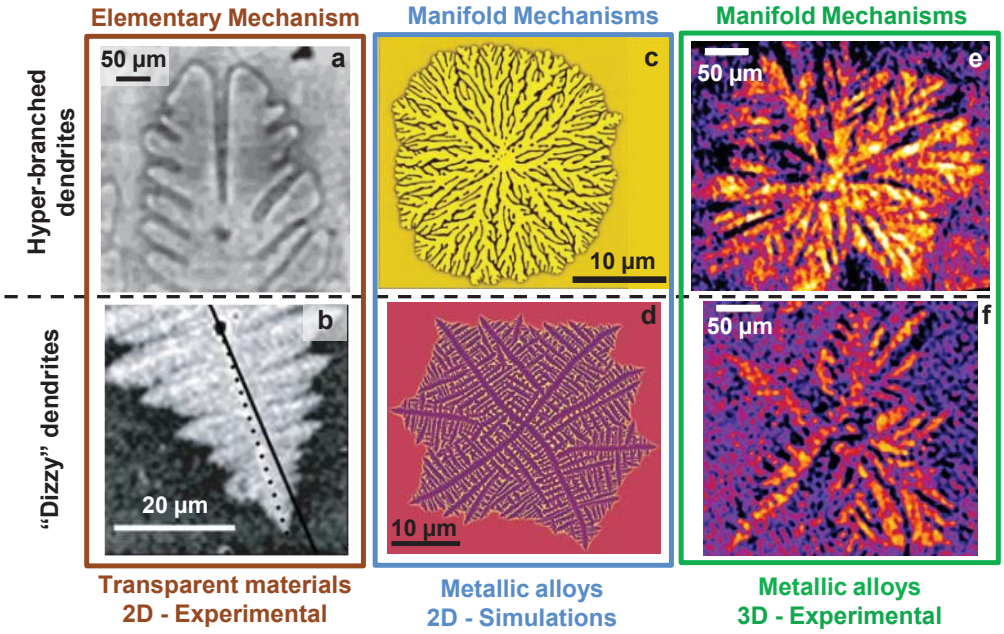

Figure 7 Temporal progression of experimental and simulated investigations of particles-induced dendrites morphologies. a and **b** illustrate elementary mechanisms revealed by 2D observations of a single particle respectively splitting **[11]** and deviating **[6]** a dendrite in transparent organics. **c** and **d** are 2D phase field simulation results obtained for metals (Ni-Cu system) **[6,7]** supporting the previously experimental evidences but this time reporting manifold mechanisms either by the presence of a large number of particles or by modification of free energy and kinetic coefficient parameter. **e** and **f** are taken from the present experiment highlighting the morphological similarities. The colour rendering is a guide to the eyes for a better contrast between solid and liquid phase. **a** is reprinted from ref **[11]** with permission, Copyright 1991, Elsevier. **b** and **d** are reprinted from ref **[6]** with permission, Copyright 2003, Nature Publishing Group. **c** is reprinted from ref **[7]** with permission, Copyright 2004 , Nature Publishing Group.

Supplementary Material

Click here to download Supplementary Material: Daudin_Supplementary_Material.docx

*Graphical Abstract

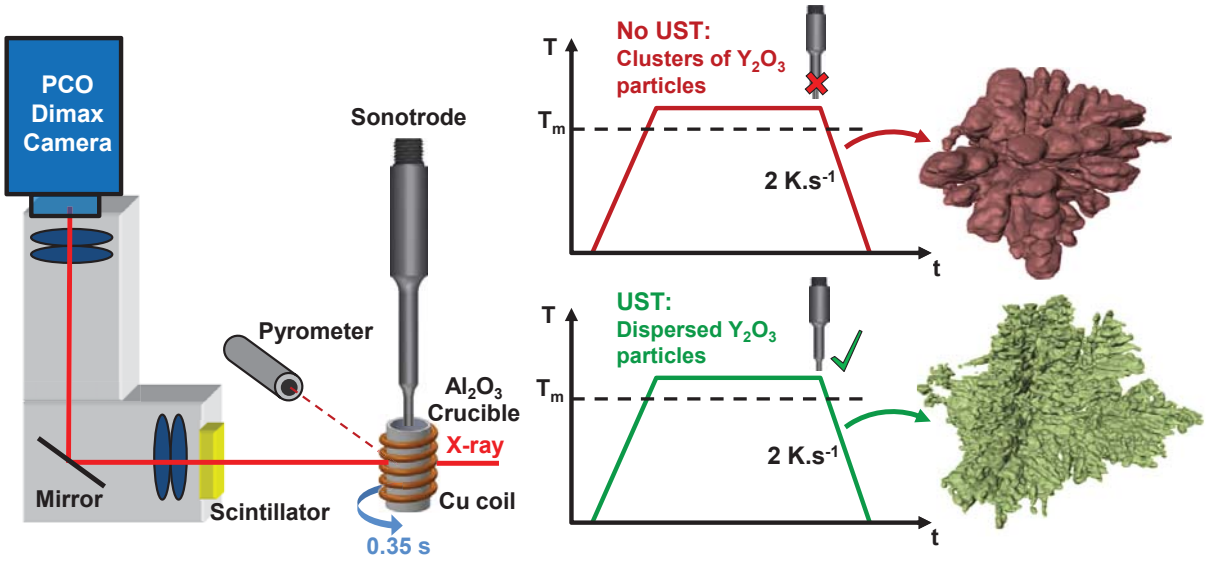

"Particle-induced morphological modification of Al alloy equiaxed dendrites revealed by sub-second *in situ* microtomography"